The Astrophysical Journal, 949:1 (9pp), 2023 May 20 https://doi.org/10.3847/1538-4357/acc9ad
© 2023. The Author(s). Published by the American Astronomical Society.
OPEN ACCESS

Spectroscopic Characterization of Diazophosphane—A Candidate for Astrophysical Observations

Martin Tschöpe and Guntram Rauhut
Institute for Theoretical Chemistry, University of Stuttgart, Pfaffenwaldring 55, Stuttgart, D-70569, Germany
Received 2023 February 16; revised 2023 March 30; accepted 2023 March 30; published 2023 May 18

Abstract

Quite recently, diazophosphane, HP−N≡N, was synthesized for the first time. This was accomplished by a reaction of PH_3 with N_2 under UV irradiation at 193 nm. As these two molecules have been observed in different astrophysical environments, as for example, in the circumstellar medium and, in particular, in the AGB star envelope IRC+10216, the question arises whether HPN_2 can be found as well. So far there is only the aforementioned experimental work, but neither rotational nor rovibrational data are available. Hence, the lack of accurate line lists, etc. to identify diazophosphane is the subject of this work, including a detailed analysis of the rotational, vibrational, and rovibrational properties for this molecule. Our calculations rely on multidimensional potential energy surfaces obtained from explicitly correlated coupled-cluster theory. The (ro)vibrational calculations are based on related configuration interaction theories avoiding the need for any model Hamiltonians. The rotational spectrum is studied between $T = 10$ and 300 K. In contrast, the partition functions for HPN_2 and DPN_2 are given and compared for temperatures up to 800 K. In addition, more than 70 vibrational transitions are calculated and analyzed with respect to resonances. All these vibrational states are considered within the subsequent rovibrational calculations. This allows for a detailed investigation of the infrared spectrum up to 2700 cm^{-1} including rovibrational couplings and hot bands. The results of this study serve as a reference and allow, for the first time, for the identification of diazophosphane, for example, in one of the astrophysical environments mentioned above.

Unified Astronomy Thesaurus concepts: Computational methods (1965); Spectral line identification (2073); Asymptotic giant branch stars (2100); Molecular data (2259); Molecular spectroscopic constants (2260); Infrared spectroscopy (2285)

1. Introduction

Since the first molecule was detected in the interstellar medium in 1937 (Dunham 1937; Swings & Rosenfeld 1937; McKellar 1940) more than 200 molecular species have been observed in the circumstellar or interstellar media (Müller et al. 2001, 2005; Endres et al. 2016; McGuire 2018). Two of these molecules are molecular nitrogen (N_2) and phosphane (PH_3). It was only in 2004, when Knauth et al. (2004) identified N_2 in the surroundings of HD 124314. Four years later, PH_3 was discovered simultaneously and independently by Agúndez et al. (2008) and Tenenbaum & Ziurys (2008).

Quite recently, Lu et al. (2022) were able to synthesize diazophosphane, HP−N≡N, for the first time. Moreover they analyzed its vibrational fundamental bands at 10 K. They obtained this species from the reaction of PH_3 with N_2 upon irradiation with UV-light at 193 nm. Since both molecules and the UV radiation are present in the circumstellar medium and can even be found in the envelope of the same AGB star IRC+10216 (Cherchneff 2012; Agúndez et al. 2014), the question arises whether HPN_2 can be found under similar conditions as well. To solve this question, highly accurate rotational, vibrational, and rovibrational spectra are of particular importance.

Although there are some studies about HPN_2 in the solid state (Ghellab et al. 2019) or as a crystalline powder (Schnick & Lücke 1992; Jacobs et al. 1997), these works refer to the isomeric form of P = N(NH). In contrast to that, we focus on the isomer HP−N≡N, which was so far only synthesized by Lu et al. (2022), as mentioned before. These authors also provide experimental frequencies for four of the six fundamental vibrational modes as well as one overtone. Additionally, they provide theoretical results for all fundamental bands and the same overtone. Other than that, no simulations of HPN_2 exist. For this reason, the demand for line lists, microwave and infrared spectra, geometrical parameters, partition functions, etc. is largely unsatisfied. This issue will be tackled within this work.

During recent decades, various approaches avoiding the need for model Hamiltonians have been developed to investigate rotational, vibrational, and rovibrational spectra by the groups of Yachmenev et al. (2011) (Yachmenev et al. 2013; Yurchenko et al. 2017; Clark et al. 2020), Nikitin et al. (2017) (Rey et al. 2017; Tyuterev et al. 2019), Carter et al. (2012) (Carter et al. 2017), Rauhut (2004) (Tschöpe et al. 2021), Smydke et al. (2019) (Ferenc & Matyus 2019; Tobias et al. 2019; Santa Daria et al. 2021), and many more (Wang & Carrington 2013; Sarka et al. 2019; Simmons et al. 2019). Some of these are based on the seminal work of Watson (1968), introducing the respective Hamiltonian. Subsequently, vibrational configuration interaction (VCI) theory (Bowman et al. 1979; Christoffel & Bowman 1982; Neff & Rauhut 2009; Pfeiffer & Rauhut 2014; Schröder & Rauhut 2022) was introduced for nonrotating molecules and after that rovibrational configuration interaction (RVCI) theory (Erfort et al. 2020a, 2020b, 2022) for the simulation of rotating molecules. These approaches rely on high-level potential energy surfaces

Original content from this work may be used under the terms of the Creative Commons Attribution 4.0 licence. Any further distribution of this work must maintain attribution to the author(s) and the title of the work, journal citation and DOI.

(PESs) (Ziegler & Rauhut 2016, 2018, 2019) for the efficient calculation of rovibrational line lists and spectra for semirigid molecules. The two main limitations for these methods are, that they lose much of their efficiency for vibrational modes with large deflections, i.e., for floppy molecules. Hence this method is very suitable for our application, since HPN_2 is a semirigid system.

In this work, we use high-level multidimensional PESs, VCI, and RVCI calculations, as implemented in the MOLPRO (Werner et al. 2020) package of ab initio programs, to determine the rovibrational spectrum of diazophosphane. Moreover, geometrical parameters as well as values for the partition functions at temperatures between 10 and 800 K will be presented. In addition, microwave and infrared spectra, vibrational line lists, and spectroscopic constants will be provided accompanied by a discussion about the influence of hot bands on the simulated spectra at different temperatures. These calculations were carried out for both HPN_2 and its deuterated isotopologue, DPN_2.

2. Theory

2.1. Rovibrational Energies

The implementation of VCI theory used in this work is based on the Watson Hamiltonian for nonrotating molecules H_{vib}, while the implementation of RVCI theory is based on the Watson Hamiltonian for rotating molecules:

$$H = \underbrace{\frac{1}{2}\sum_{\alpha\beta}\pi_\alpha\mu_{\alpha\beta}\pi_\beta - \frac{1}{2}\sum_i\frac{\partial^2}{\partial q_i^2} - \frac{1}{8}\sum_\alpha\mu_{\alpha\alpha} + V(\boldsymbol{q})}_{H_{\mathrm{vib}}} + \underbrace{\frac{1}{2}\sum_{\alpha\beta}\mu_{\alpha\beta}J_\alpha J_\beta}_{H_{\mathrm{rot}}} - \underbrace{\frac{1}{2}\sum_{\alpha\beta}(J_\alpha\mu_{\alpha\beta}\pi_\beta + \pi_\alpha\mu_{\alpha\beta}J_\beta)}_{H_{\mathrm{rv}}} \quad (1)$$

The use of the Born–Oppenheimer approximation yields the PES, V, depending on the normal coordinates q_i. Equation (1) also depends on the Cartesian components of the angular momentum operator, J_α, and the vibrational angular momentum (VAM) operator

$$\pi_\alpha = -i\sum_{jk}\zeta_{jk}^{\alpha}q_j\frac{\partial}{\partial q_k}. \quad (2)$$

Thereby ζ_{jk}^{α} corresponds to an element of the antisymmetric Coriolis ζ-constant tensor, with Cartesian elements $\alpha, \beta \in \{x, y, z\}$. For the following discussion, it is favorable to split the Watson Hamiltonian in the following three parts: the pure vibrational term H_{vib}, the rotational term H_{rot}, and the Coriolis-coupling term H_{rv}. The inverse of the effective moment of inertia tensor is denoted by μ, see Watson (1968). Both, μ and the potential V, rely on an n-mode expansion (Bowman et al. 2008) and an analytic sum-of-products representation being obtained from efficient Kronecker product fitting (Ziegler & Rauhut 2016). In order to obtain rovibrational energies and intensities, a two-step process is used. First, the Schrödinger equation for the Hamiltonian of a nonrotating molecule H_{vib} is solved by VCI theory, yielding pure vibrational energies and the corresponding wave functions:

$$|\Phi_v\rangle = \sum_I c_I|\phi_v^I\rangle. \quad (3)$$

To determine the vibrational wave functions $|\Phi_v\rangle$ in a compact form, an initially large number of Hartree products $|\phi_v^I\rangle$ (configurations) is screened within a configuration-selective VCI approach (Mathea & Rauhut 2021; Mathea et al. 2022).

Second, the Schrödinger equation for the Hamiltonian of rotating molecules (see Equation (1)) is solved by RVCI theory. The basis functions are provided by a direct product of the VCI wave functions and pure rotational basis functions $|\Phi_r\rangle$. This yields rovibrational wave functions of the form:

$$|\Psi_{\mathrm{rv}}\rangle = \sum_{rv} c_{rv}|\Phi_r\rangle|\Phi_v\rangle. \quad (4)$$

Within this work, molecule-specific rotational basis (MSRB) functions for $|\Phi_r\rangle$ have been employed, as they allow for a particular robust quantum number assignment. The MSRB is a linear combination of Wang combinations (Špirko et al. 1985) and is determined by solving the rotational Schrödinger equation for the vibrational ground state (Erfort et al. 2020a).

2.2. Infrared Intensities

Rovibrational infrared line intensities can be obtained by

$$I = \frac{2\pi^2 N_{\mathrm{A}}}{3\epsilon_0 h^2 c^2}\frac{e^{-E''/kT}(1 - e^{-(E'-E'')/kT})}{Q(T)}(E' - E'')R. \quad (5)$$

They depend on a prefactor consisting of natural and physical constants, the square of the transition moment R and a temperature-dependent prefactor, describing the thermal occupation of the rovibrational states involved in the transition. The energies of the initial and final states are given by E'' and E', respectively. The rovibrational partition function $Q(T)$ depends on the temperature and can be computed by

$$Q(T) = \sum_{\mathrm{rv}} g_{\mathrm{rv}}e^{-E_{\mathrm{rv}}/k_{\mathrm{B}}T}, \quad (6)$$

where the summation considers all rovibrational states rv. E_{rv} denotes the corresponding energies and g_{rv} the corresponding degeneracies. The latter is a product of the nuclear spin statistical weight (NSSW) g_{ns} and the degeneracy factor $2J + 1$ originating in the absence of electric and magnetic fields. Since diazophosphane shows C_s symmetry, the two NSSWs are identical, with a value of 36 for HPN_2 and 54 for DPN_2.

2.3. Computational Details

To determine the equilibrium geometry, the harmonic frequencies as well as the corresponding normal coordinates for diazophosphane, explicitly correlated coupled-cluster theory including single and double excitations, and a perturbative treatment of the triple excitations, CCSD(T)-F12b has been used (Adler et al. 2007). Two PESs have been calculated for each of the isotopologues. The first PES uses the frozen core (fc) approximation, which relies on error compensation with respect to neglected contributions to the electronic energy, as for example, relativistic effects, diagonal Born–Oppenheimer corrections, high-order coupled-cluster terms, and core-correlation contributions. This error compensation usually leads to nicely matching vibrational frequencies in comparison to experimental results. For this reason, this approximation is often used to calculate rovibrational line lists, spectra, and partition functions. The second PES was obtained by all-electron (ae) correlation calculations, which

explicitly account for core–core and core–valence interactions, since the work of Schneider & Rauhut (2022) has shown, that at least for the determination of spectroscopic constants this approach leads to slightly better results. In most of our analyses, we compare the results obtained from these two different PESs to narrow the range where experimental values could be expected.

While in the work of Lu et al. (2022), an orbital basis set of triple-ζ quality, i.e., cc-pVTZ-F12 (Peterson et al. 2008) was used, slightly larger orbital bases of quadruple-ζ quality, i.e., cc-pVQZ-F12 and cc-pcVQZ-F12, have been employed here. The all-electron explicitly correlated coupled-cluster calculations require an adjustment of the different γ exponents for the Slater geminal functions as recommended by May & Manby (2004). Consequently, the core–core, core–valence, and valence–valence orbital pair values were set to 0.8, 1.7, and 2.2, respectively. In contrast to that, a common exponent of $\gamma = 1.0$ was used within the frozen core calculations. Moreover, the complementary auxiliary basis set correction was added to the total energies (Adler et al. 2007; Knizia & Werner 2008).

All multidimensional PESs were represented by an n-mode expansion truncated after the four-mode coupling terms (Bowman et al. 2008). A multilevel scheme, as introduced by Pflüger et al. (2005), has been used throughout the calculations. More precisely, the 1D and 2D surfaces have been calculated at the same level of accuracy that was used for the determination of the equilibrium geometry and harmonic frequencies. In contrast, for the 3D and 4D contributions, a smaller basis set of triple-ζ quality has been used. A likewise multilevel scheme, but being based on calculations using the distinguishable clusters (DCSD) approximation (Kats & Manby 2013), has been used for determining the dipole moment surface (DMS). Runtime savings due to symmetry have been exploited twofold: within the electronic single point calculations and for the terms of the n-mode expansion (Ziegler & Rauhut 2018). The grid representations of the multidimensional surfaces have been transformed by Kronecker product fitting to an analytical sum-of-products representation based on nine monomials per mode.

Vibrational wave functions have been obtained from state-specific configuration-selective VCI theory (Mathea & Rauhut 2021; Mathea et al. 2022; Schröder & Rauhut 2022). The basis set used in these calculations is symmetry adapted and relies on Hartree products (configurations) being generated from one-mode wave functions (modals), which have been determined from ground-state based vibrational self-consistent field (VSCF) theory. A set of 18 mode-specific distributed Gaussians and a constant μ-tensor has been used within the VSCF calculations. The correlation space within the VCI calculations has been restricted twofold: The maximum number of vibrational quantum numbers was set to 15 and a maximum excitation per mode up to the sixth root was used. Moreover, the maximum number of simultaneously excited modes was chosen to be six, so there is no restriction in this respect. All these values do not refer to the ground state, but are relative to the leading configuration of the vibrational state of interest. This resulted in about 3×10^4 configurations per irreducible representation and thus we consider the final VCI results to be close to the full VCI limit. A μ-tensor expansion up to first order was used for the diagonal elements of the VCI matrix. In contrast, all other matrix elements are limited to a constant μ-tensor. A residuum based eigenvalue solver (RACE) has been employed for the determination of the eigenenergies of predefined states (Petrenko & Rauhut 2017).

The RVCI calculations use a maximum angular momentum number of $J_{max} = 75$ for the calculations of the line list and $J_{max} = 100$ for the determination of the partition function. A temperature range of 10–300 K has been chosen for the rovibrational spectra, while the partition functions are provided for temperatures up to 800 K. This covers the experimental conditions of Lu et al. (2022; 10 K), terrestrial conditions for further lab experiments and some astrophysical areas, for example the outer regions of the circumstellar medium. The latter have been determined from a sum of RVCI state energies, i.e., no separability approximation has been used. For the evaluation of the rotational integrals originating from the Watson Hamiltonian, a second-order μ-tensor is used, while a first order μ-tensor is used for the Coriolis-coupling contributions. Based on a similar convergence analysis as shown in our previous work (Tschöpe & Rauhut 2022) these truncations of the n-mode expansions appear to be justified.

The rovibrational basis functions are provided by a direct product of VCI wave functions and molecule-specific rotational basis (MSRB) functions (see Equation (4)), as explained in detail by Erfort et al. (2020a). The basis set size for the vibrational subspace was limited by two criteria: the maximum vibrational transition frequency was chosen to be smaller than 5000 cm^{-1} and the maximum sum of vibrational quantum numbers was set to be less than 4. This yields $N_{vib} = 73$ vibrational states for HPN_2 and $N_{vib} = 80$ states for DPN_2. Since the maximum size of the rotational basis set is given by $2J_{max} + 1 = 151$ for the calculation of rovibrational spectra, the largest matrix is of size $N_{rovib} = 12{,}080$. For HPN_2, the resulting wall clock time for the combined VCI and RVCI calculations was ≈33 hr on six CPU (central processing units) cores. While the VCI calculations contributed less than 1% and the calculation of the RVCI energies and wave functions about 15%, most of the time is spent for the calculation of the RVCI intensities. For DPN_2, longer calculation times by about 50% were needed due to the larger number of vibrational basis functions, which increases the CPU time in two ways: by a larger number of rovibrational transitions and larger RVCI wave function vectors. Within the RVCI calculations, ≈50 million transitions for HPN_2 and ≈100 million transitions for DPN_2 have been considered. The printout was filtered to ≈161,000 and ≈404,000 transitions for HPN_2 and DPN_2, respectively. The main selection criterion was an intensity of at least 10^{-4} relative to the strongest transition in the spectrum for $T = 300$ K.

3. Results and Discussion

3.1. Geometrical Parameters

Calculated geometrical parameters are presented in Figure 1. Parameters obtained by Born–Oppenheimer equilibrium geometries are denoted $\boldsymbol{r}_e$. Since the equilibrium geometry is not affected by deuteration, this column is not explicitly given for DPN_2. In addition, two different types of vibrationally averaged geometrical parameters, $\boldsymbol{r}_a$ and $\boldsymbol{r}_g$, are provided. Averaging the atomic positions over the VCI ground-state wave function yields the former. The latter uses the expectation value of the bond lengths expressed in normal coordinates to calculate instantaneous internuclear distances. It is well known (Czakó et al. 2009; Dinu et al. 2020; Tschöpe et al. 2021;

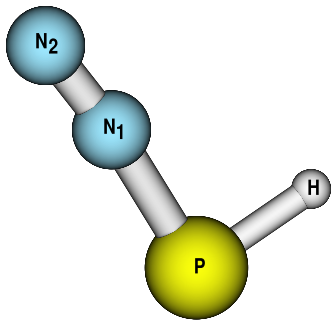

	fc					ae		
	HPN_2			DPN_2		HPN_2		
Coord.	r_e	r_a	r_g	r_a	r_g	r_e	r_a	r_g
$r(N_2N_1)$	1.126	1.125	1.130	1.125	1.130	1.123	1.123	1.128
$r(N_1P)$	1.698	1.706	1.708	1.706	1.708	1.692	1.700	1.702
r(PH)	1.415	1.428	1.436	1.424	1.429	1.412	1.425	1.432
$\alpha(N_2N_1P)$	173.8	173.8		173.9		173.8	173.9	
$\alpha(N_1PH_1)$	88.8	89.0		88.9		88.8	89.0	

Figure 1. Computed Geometrical Parameters of Diazophosphane Bond lengths are given in Å and angles are given in degrees. Comparison between explicitly correlated coupled-cluster surfaces CCSD(T)-F12b based on the frozen core (fc) approximation with a cc-pVQZ-F12 basis set and all-electron (ae) correlation calculations with a cc-pcVQZ-F12 basis set. For DPN_2, equilibrium geometries are not explicitly given since they are identical for both isotopologues.

Tschöpe & Rauhut 2023) that these two approaches can yield significantly different results. Compared to these previous works, this effect is smaller for diazophosphane than for other molecules. This is not surprising, as the largest differences were observed for CH bond lengths (Tschöpe et al. 2021; Tschöpe & Rauhut 2023), which are not present in diazophosphane. However, the largest absolute difference between $\boldsymbol{r}_a$ and $\boldsymbol{r}_g$ was again found for the bond involving hydrogen, i.e., $\Delta\ r(\mathrm{PH}) = 0.008$ Å. Comparing the results for HPN_2 and DPN_2 shows, on the one hand, that obviously the bond length r (PH) and r(PD), respectively, changes the most, but also that the angle involving water $\alpha(N_1PH_1)$ changes only marginally. Figure 1 also provides a comparison between calculations based on a PES relying on the frozen core approximation (fc) and another PES relying on all-electron (ae) correlation calculations. The difference between fc and ae calculations varies between 0.002 and 0.006 Å, with an expected and systematic trend toward smaller bond lengths for the ae calculations.

3.2. Partition Function

As mentioned before, the partition function has been determined by direct summation. A temperature range between 10 and 800 K has been chosen in order to consider a variety of astrophysical areas, the experimental conditions of Lu et al. (2022), and terrestrial conditions for further lab experiments. The results for both isotopologues of diazophosphane can be found in Table 1 and in Figure 2. The double logarithmic plot shows the same near-linear behavior as previously observed for other molecules (Martin et al. 1992; Harris et al. 1998; Vidler & Tennyson 2000). Up to a temperature of ≈300 K, the trend is almost exactly linear. However, at 300 K, a small increase in the slope arises. As discussed by Amyay et al. (2011), this effect can be caused by an increased state density, e.g., due to thermal occupation of excited vibrational bands, while a not properly converged summation would lead to a decreasing slope. The partition function for DPN_2 is about a factor of 2.1 larger than for HPN_2. The fact that the NSSWs of DPN_2 are 1.5 times larger than for HPN_2, explains some part of this effect. Moreover, due to the higher mass of DPN_2 the state energies decrease and thus show higher occupations for a fixed temperature, as can be seen from Equation (6).

3.3. Vibrational Transitions

Within our RVCI calculations, we considered 73 vibrational states for HPN_2 and 80 for DPN_2. The results for the fundamental bands and overtones for both isotopologues are shown in Table 2. Results for combination bands are given in the supplementary material. As has been explained before, we provide a comparison between calculations based on a PES relying on the frozen core (fc) approximation and an all-electron (ae) correlation PES. As expected and previously observed for other molecules, the deviations between fc and ae results are smaller for fundamental bands than for overtones. Moreover, the relative deviations in the intensities are relatively small in most cases, except for $2\nu_2$, for which the all-electron calculation yields an approximately 50% higher intensity. Comparing our simulated results with the experimental results of Lu et al. (2022) shows a slightly better agreement with the frozen core calculation frequencies. However, the standard deviation is fairly high due to outliers and the small sample size of only five transitions. Moreover, it should be considered that Lu et al. (2022) used matrix spectroscopy, whereas our simulations refer to the gas phase.

Comparing the frequencies of the fundamental bands of HPN_2 and DPN_2 shows the expected strong deuteration effects for the H−P stretching and bending modes. Note that ν_1 is the H−P stretching mode for HPN_2 and ν_2 is the N≡N stretching mode. This is reversed for DPN_2, which can easily be seen by considering the intensities. Moreover, the H−P bending mode, ν_3, is shifted by about 220 cm^{-1} and loses about 50% of its

Table 1
Partition Functions for HPN_2 and DPN_2 for Different Temperatures

T (K)	Q	
	HPN_2	DPN_2
5	7.34×10^2	1.53×10^3
10	2.05×10^3	4.37×10^3
20	5.83×10^3	1.24×10^4
35	1.35×10^4	2.87×10^4
50	2.31×10^4	4.90×10^4
75	4.25×10^4	9.03×10^4
100	6.59×10^4	1.40×10^5
150	1.27×10^5	2.72×10^5
200	2.15×10^5	4.64×10^5
300	5.15×10^5	1.14×10^6
500	1.97×10^6	4.38×10^6
800	7.26×10^6	1.60×10^7

Note. RVCI calculations are based on a PES using the frozen core approximation because it yields vibrational frequencies closer to potential experimental results.

Table 2
Vibrational Fundamental Bands and Overtones of Diazophosphane

Band	Irrep	HPN_2					DPN_2	
		ν			I		ν	I
		fc	ae	Ref. 1	fc	ae	fc	
ν_1	A'	2315.2	2320.0	2322.1	35.7	37.2	2030.3	467.4
ν_2	A'	2030.0	2036.5	2022.7	469.9	471.3	1682.7	18.0
ν_3	A'	934.3	938.9	935.2	16.2	16.4	712.4	8.2
ν_4	A'	576.9	580.5	574.4	24.8	24.5	575.7	25.0
ν_5	A''	440.8	443.7	n.o.	1.9	1.9	433.8	1.9
ν_6	A'	354.0	356.5	n.o.	2.3	2.3	333.2	2.2
$2\nu_1$	A'	4545.6	4555.1	n.o.	0.1	0.1	4029.6	3.1
$2\nu_2$	A'	4030.8	4042.6	4045.4	2.2	3.2	3322.5	0.1
$2\nu_3$	A'	1866.2	1874.6	n.o.	0.2	0.2	1424.4	0.1
$2\nu_4$	A'	1135.6	1142.7	n.o.	0.0	0.0	1133.7	0.0
$2\nu_5$	A'	880.3	886.0	n.o.	1.1	1.1	866.5	1.1
$2\nu_6$	A'	705.7	710.7	n.o.	1.3	1.3	665.8	1.1
$3\nu_3$	A'	2794.2	2806.1	n.o.	0.0	0.0	2134.9	0.0
$3\nu_4$	A'	1675.6	1686.4	n.o.	0.2	0.2	1673.2	0.1
$3\nu_5$	A''	1321.4	1329.9	n.o.	0.0	0.0	1299.7	0.0
$3\nu_6$	A'	1061.5	1069.0	n.o.	0.0	0.0	1002.8	0.0

Note. Comparison between VCI results of HPN_2 for the PES using the frozen core (fc) approximation and the all-electron (ae) correlation calculation. Frequencies ν are given in cm^{-1} and infrared intensities I are given in km mol^{-1}. Irreducible representations (irrep) are provided for each state.
References. (1) Experimental matrix spectroscopy by Lu et al. (2022).

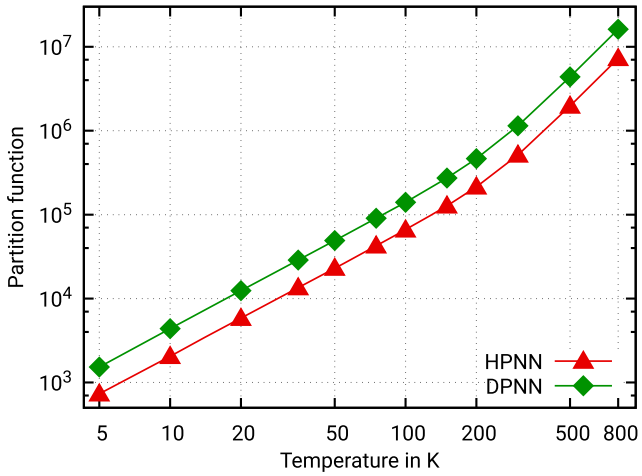

Figure 2. The partition function of diazophosphane for different temperatures.

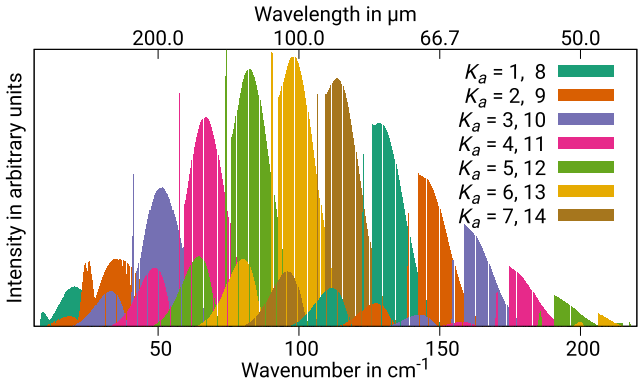

Figure 3. Vibrational ground-state stick spectrum of diazophosphane for 300 K. The color of the transitions are defined by the K_a quantum number of the upper state. For the sake of clarity, hot bands are not shown. The maximum total angular momentum was set to $J = 75$.

intensity. All of these findings are in good agreement with the analysis in Lu et al. (2022).

Since resonances are intrinsically accounted for in VCI theory, an analysis of resonating states is straightforward and is provided in our calculations once a configuration contributes more than 10% to the state of interest. Among the considered vibrational bands, there are only a small number of meaningful resonances. Neither the fundamental bands nor the overtones for HPN_2 and DPN_2 show any Fermi (Fermi 1931) or Darling–Dennison (Darling & Dennison 1940) resonances. The only coupling for an overtone of HPN_2 can be found for $2\nu_2$ and $\nu_2 + 2\nu_4 + 2\nu_5$ at about 4030 cm^{-1}. Moreover, the combination band $\nu_3 + \nu_5$ shows a strong resonance with $\nu_4 + \nu_5 + \nu_6$ at 1375 cm^{-1} (see the supplementary material). However, since neither of the two bands involved has a noticeable intensity, experimental confirmation of the latter resonance is not possible.

3.4. Rotational Spectrum

The pure rotational spectrum at a temperature of 300 K for diazophosphane is provided by Figure 3. Hot bands are not shown in this figure for two reasons: First, it allows for a better analysis of the spectrum. Second, they will be discussed in detail later on. The color coding in Figure 3 visualizes the assigned K_a quantum number of the initial rovibrational state. The first progressions between 5 and 25 cm^{-1} shown in dark green correspond to $K_a = 1$, the orange progressions denote $K_a = 2$, and so on. The color pattern repeats after the seventh color, hence the dark green progressions at 125 and 150 cm^{-1} correspond to $K_a = 8$. The fact that each progression is given in a single color shows that the assignment of the quantum number K_a is consistent for the vibrational ground state. Moreover, for each K_a value, the coloring allows us to identify the thin but dense Q-branch in the center, the strong R-branch

at the rhs, and the much weaker P-branch at the lhs. However, it should be noted that, for $K_a = 1$ and $K_a > 11$, only two branches are clearly visible.

A study of the temperature-dependent effect of the spectrum including hot bands is shown in Figure 4. The previously discussed Figure 3 corresponds to the black transitions of the bottom panel in Figure 4. In addition, this figure shows three different hot bands ($4^1 \rightarrow 4^1$, $5^1 \rightarrow 5^1$, $6^1 \rightarrow 6^1$) all given in red.

Up to a temperature of 100 K, ignoring hot bands is a decent approximation. At 200 K, the contribution of hot bands is about one order of magnitude smaller than for the ground-state transitions and is almost entirely driven by the $6^1 \rightarrow 6^1$ transitions. Moreover, even in cases where hot bands contribute more strongly to the overall appearance of the rotational spectrum, i.e., at 300 K, this does not lead to a shift in intensities toward higher or lower frequencies. This is in contrast to other molecules (Tschöpe & Rauhut 2023) and other parts of the diazophosphane spectrum (see Section 3.6).

3.5. Rovibrational Spectrum

An overview of the rovibrational infrared spectrum of diazophosphane for a temperature of 300 K and spectral range up to 2700 cm^{-1} is provided in Figure 5. In contrast to Figure 3, here the color coding refers to the vibrational states involved. More precisely, for the transitions in orange, both the initial and final vibrational quantum numbers correspond to the vibrational ground state. The dark green lines denote vibrational fundamental bands (e.g., ν_6). First overtones (e.g., $2\nu_6$) and second overtones (e.g., $3\nu_6$) are shown in yellow and light green, respectively. As mentioned before, we have restricted the RVCI configuration space to vibrational states up to a maximum sum of quantum numbers of 3, i.e., third overtones and combination bands of four different vibrational transitions are not included. The fact that there is only one very weak second overtone at 1650 cm^{-1} and the absence of strong second overtones in Table 2 provide some evidence that this is a good approximation. Further analysis shows that, in this spectral region, the coupling between these higher overtones and other strong vibrational bands is relatively weak compared to the two or three mode combination bands, which are colored pink and gray, respectively. Finally, all types of hot bands are colored black.

As expected from Table 2, the ν_2 mode is the most intense vibrational transition by more than one order of magnitude. Although ν_2 and $\nu_3 + 2\nu_4$ have the same irreducible representation (A'), their coupling within VCI theory is virtually zero, but within RVCI theory it is noticeable. This can also be seen by considering the intensities. VCI calculations yield an intensity of 469.9 km mol^{-1} for ν_2 and 0.4 km mol^{-1} for $\nu_3 + 2\nu_4$. In contrast to that, the RVCI results show a little less than two orders of magnitude difference in the intensities, see Figure 5. Moreover, there are several regions that are sufficiently separated to allow for independent investigations by different experiments.

A more detailed analysis of some spectral regions of the infrared spectrum of diazophosphane is provided in Figure 6. All of the strong bands shown in the different panels are fundamental bands of this near-prolate asymmetric top molecule. Since panel (a) shows two strong bands, all of the six fundamental bands are covered within this figure. Neither of the two vibrational modes in panel (a) can be assigned to a

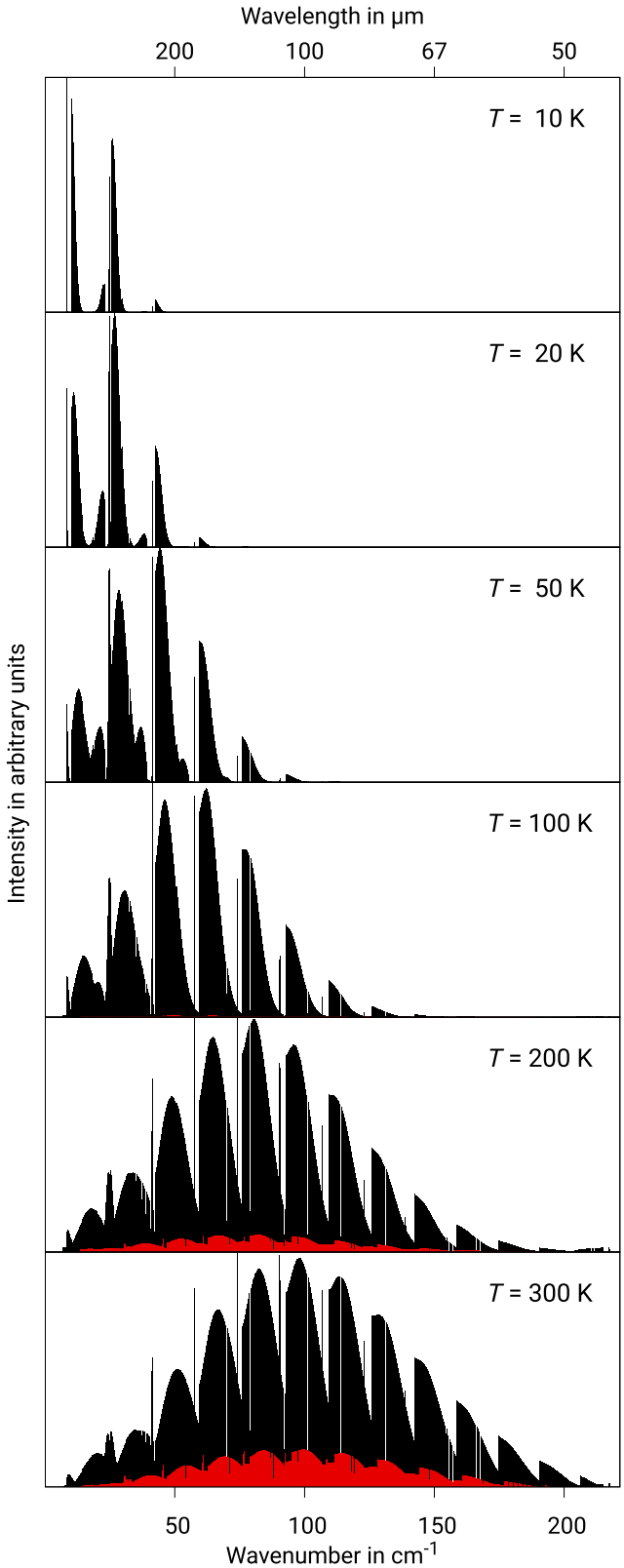

Figure 4. Vibrational ground-state stick spectrum of diazophosphane for different temperatures. Transitions from the vibrational ground state to the vibrational ground state are drawn in black. All hot band transitions are given in red. The maximum total angular momentum was set to $J = 75$.

typical asymmetric top band type. While the in-plane P−N≡N bending mode ν_6 shows a similarly strong change in the electric dipole moment along the A- and B-axes, the dipole moment of

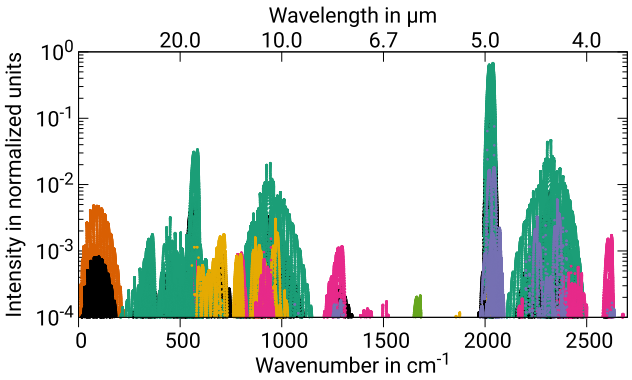

Figure 5. Overview of the rovibrational infrared stick spectrum of diazophosphane at a temperature of 300 K. Hot bands are colored black, the pure rotational spectrum is given in orange, fundamental bands in dark green, first overtones in yellow, second overtones in bright green (only visible at 1650 cm^{-1}). Combination bands of two or three different vibrational transitions are colored pink or gray, respectively. The maximum total angular momentum quantum number is set to $J = 75$.

the out-of-plane P−N≡N bending mode ν_5 changes only along the *C*-axis. However, the small spectral separation of the two bands of less than 100 cm^{-1} and the fact that they belong to different irreps lead to strong Coriolis-coupling and hence a lifting of the typical selection rules.

The P−N stretching mode ν_4 shows the expected A-type spectrum. However, it is subject to intensity borrowing due to coupling with the much weaker overtones $2\nu_5$ and $2\nu_6$. As discussed in Tschöpe et al. (2021) and Tschöpe & Rauhut (2023), this leads to the typical compression of the branch facing the borrowing bands, i.e., toward higher energies, in this case. Another typical example of an A-type pattern arises for ν_2, which was to be expected since it is assigned to the N≡N stretching mode. Although there are combination bands coupling with ν_2, this leads to only a small asymmetry. The H−P bending mode ν_3 in panel (c) and H−P stretching mode ν_1 in panel (e) show the expected B-type intensity pattern.

3.6. Hot Bands

The influence of hot bands on the low-frequency region below 600 cm^{-1} can be seen in Figure 7. Panel (a) shows the vibrational ground-state spectrum and the fundamental modes ν_6 and ν_5, while panel (b) shows ν_4. At a temperature of 300 K, there are three vibrational states with meaningful thermal occupations, which are 4^1, 5^1, and 6^1. The hot bands of the pure rotational spectrum were already briefly discussed in Section 3.4. Considering the different transitions $4^1 \rightarrow 4^1$, $5^1 \rightarrow 5^1$, and $6^1 \rightarrow 6^1$ individually allow for two results: (1) the intensity pattern is mainly the same in all cases and (2) the intensity ratios seems to be in accordance with the thermal occupation ratios.

In contrast to that, the four transitions $0 \rightarrow 6^1$, $6^1 \rightarrow 6^2$, $5^1 \rightarrow 5^1 + 6^1$, and $4^1 \rightarrow 4^1 + 6^1$ at around 350 cm^{-1} show very different intensity patterns. Especially, the $5^1 \rightarrow 5^1 + 6^1$ band in pink is significantly shifted toward higher frequencies. This effect is even more pronounced for the next higher fundamental band at 440 cm^{-1}, where all bands have a very unique visual appearance due to the strong coupling. Moreover the $5^1 \rightarrow 5^2$ transition (pink) is at least as intense as the $6^1 \rightarrow 5^1 + 6^1$ transition (green), although the thermal occupation of 5^1 is lower than for 6^1. Figure 7(b) highlights another common phenomenon for hot bands, which is a significant shift in the band center. In the case of the $4^1 \rightarrow 4^2$ band (yellow), the transition is 20 cm^{-1} lower than for the fundamental transition $0 \rightarrow 4^1$.

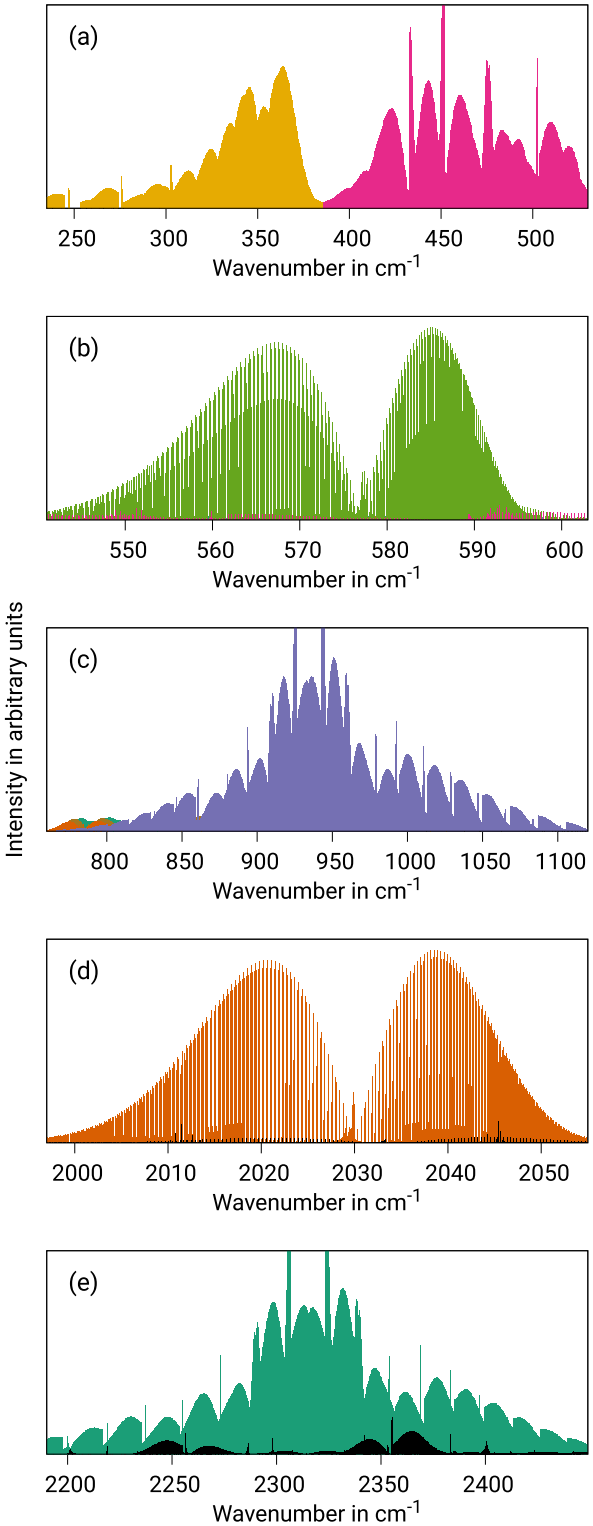

Figure 6. Infrared spectrum of the vibrational fundamental bands of diazophosphane at a temperature of 300 K. The maximum total angular momentum was set to $J = 75$. The modes ν_6 (yellow) and ν_5 (pink) are shown in panel (a), mode ν_4 (vibrant green) in (b), mode ν_3 (hazy blue) in (c), mode ν_2 (orange) in (d), and mode ν_1 (green) in (e). The *y*-axis scale range for the different figures varies.

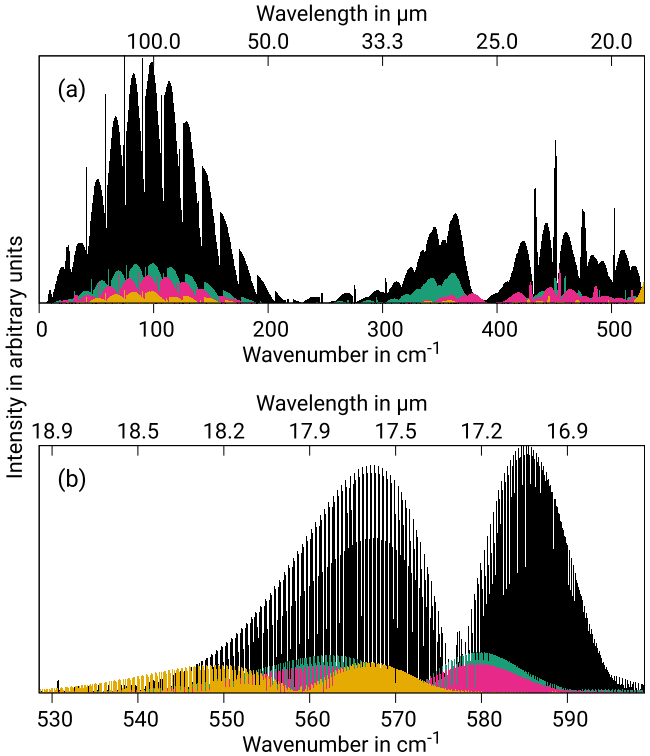

Figure 7. Infrared low-frequency stick spectrum of diazophosphane. This spectral region is split in two panels for better visibility because the band around 577 cm^{-1} is one order of magnitude stronger (see Figure 5) than the band in panel (b). For transitions drawn in black the initial vibrational state is the ground state. Hot bands for different vibrational transitions are given in different colors. Transitions initiated from vibrational state 4^1, 5^1, and 6^1 are colored yellow, pink, and green, respectively. The maximum total angular momentum was set to $J = 75$.

3.7. Spectroscopic Constants

Another way to analyze rovibrational characteristics besides comparing line lists and the visual appearance of spectra are spectroscopic constants. They allow to condense large line lists, which are obtained by experiments or simulations, into a small set of well-defined molecule-specific constants by using a model Hamiltonian. Computationally, these rotational and centrifugal distortion constants can be obtained by vibrational perturbation theory (VPT). For this reason, the PESs of HPN_2 and DPN_2 have been transformed to a quartic force field to obtain the force constants needed for VPT2 calculations. For diazophosphane, we have chosen the A-reduced Hamiltonian over its alternative, the S-reduced Hamiltonian similar to our previous studies, see Dinu et al. (2022) and Tschöpe & Rauhut (2023). Moreover, we followed the convention to use the I^r orientation for this near-prolate asymmetric top molecule.

The results for HPN_2 are given in Table 3 and, for DPN_2, they can be found in the supplementary material. Again, we provide a comparison between calculations based on a PES using the frozen core approximation and a PES obtained by all-electron calculations. Since diazophosphane is a near-prolate asymmetric top molecule, it has one very large rotational constant, i.e., A, and two rather small ones being very similar in size, B and C. The relative deviation between the fc and ae results are about 0.5%, which is similar to the findings in Schneider & Rauhut (2022). Although the quartic and especially sextic constants are several orders of magnitude smaller, the relative deviations are about the same as for the rotational constants. In fact, in many cases, the difference is about 0.1%. However, it should be mentioned that, for the sextic constants, we do not expect that the small difference between our two simulations reflects the error margin of our method.

Table 3
Spectroscopic Constants for the Vibrational Ground State of HPN_2

Parameter		ae	fc
A	[GHz]	254.46592	253.29347
B	[GHz]	5.94814	5.91260
C	[GHz]	5.80568	5.77117
Δ_J	[kHz]	2.298	2.295
Δ_{JK}	[kHz]	126.733	125.805
Δ_K	[MHz]	19.120	19.061
δ_J	[Hz]	54.842	54.748
δ_K	[kHz]	77.312	76.986
Φ_J	[Hz]	−0.002	−0.002
Φ_{JK}	[Hz]	0.432	0.430
Φ_{KJ}	[Hz]	−134.311	−135.313
Φ_K	[kHz]	−8.868	−9.050
ϕ_J	[mHz]	−0.048	−0.049
ϕ_{JK}	[Hz]	0.247	0.245
ϕ_K	[Hz]	378.121	378.626

Note. Watson's A-reduced Hamiltonian and I^r representation is used for the VPT2 calculations. Comparison between results for the PES using the frozen core (fc) approximation and the all-electron (ae) correlation calculation. The rotational constants for the equilibrium geometry are $A_e = 254.98012$ GHz, $B_e = 5.94287$ GHz, and $C_e = 5.80751$ GHz within the fc approximation and $A_e = 256.16949$ GHz, $B_e = 5.97837$ GHz, and $C_e = 5.84203$ GHz for the ae correlation calculations.

4. Summary and Conclusions

Within this work, high-level ab initio methods have been used for the first time to investigate the rotational and rovibrational spectra of diazophosphane. Explicitly correlated coupled-cluster calculations have been used to determine multidimensional PESs represented by an n-mode expansion up to fourth order. For each of the two isotopologues (HPN_2 and DPN_2), two PESs were determined. The first one uses the frozen core approximation relying on error compensation with respect to neglected contributions within the electronic energies and leads to vibrational frequencies that usually match nicely with experimental results. The second PES uses all-electron calculations, which have shown a better agreement for the spectroscopic constants in the past (Schneider & Rauhut 2022; Tschöpe & Rauhut 2023). To determine the vibrational and rovibrational frequencies and intensities, VCI and RVCI theory has been used. All simulations were performed with the MOLPRO program package of ab initio programs.

Theoretical results for the geometrical parameters of the equilibrium and vibrational averaging structures of HPN_2 and DPN_2 have been provided. Moreover, theoretical values for the partition functions within a temperature range between 10 and 800 K have been presented. In addition to that, we provided line list for more than 70 vibrational bands, which show neither Fermi nor Darling–Dennison resonances. However, it revealed a strong resonance with a leading coefficient for the VCI wave function of 0.71 for the combination bands $\nu_3 + \nu_5$ and $\nu_4 + \nu_5 + \nu_6$ at 1375 cm^{-1} for HPN_2. In contrast to HPN_2, the deuterated system shows even fewer resonances. The rotational spectrum was also studied for temperatures between 10 and 300

K, including hot bands. Moreover, we discussed the K_a quantum number dependence of the progressions. The rovibrational spectrum was analyzed with respect to the hot bands and vibrational quantum numbers. Furthermore, a discussion of the rovibrational infrared stick spectra was presented for all fundamental bands of HPN_2. Last, we provided the rotational and centrifugal distortion constants obtained by VPT calculations of the asymmetric top molecule. A comparison between results based on the all-electron PES with results obtained by frozen core calculations showed a relative deviation of about 0.5%.

These data should allow to guide observations of diazophosphane in astrophysical environments, like, for example, AGB star envelopes, as well as further laboratory studies. In particular, the spectral region between 300 and 550 cm^{-1} appears to be fairly unique and thus characteristic for the molecule's identification.

We are grateful to Prof. X. Zeng for bringing this molecule to our attention. We thank the Deutsche Forschungsgemeinschaft (DFG; project Ra 656/23-3) and the Studienstiftung des deutschen Volkes for financial support. The authors acknowledge further support by the state of Baden–Württemberg through bwHPC and the DFG through grant No. INST 40/575-1 FUGG (JUSTUS 2 cluster). This publication was funded by the German Research Foundation (DFG) grant "Open Access Publication Funding/2023-2024/University of Stuttgart" (512689491).

Software: MOLPRO (Werner et al. 2020).

Data Availability

The data that support the findings of this study, i.e., potential energy surfaces and line lists, are available online on the ZENODO database: doi:10.5281/zenodo.7628591.

ORCID iDs

Martin Tschöpe https://orcid.org/0000-0001-9888-4577
Guntram Rauhut https://orcid.org/0000-0003-0623-3254

References

Adler, T. B., Knizia, G., & Werner, H.-J. 2007, JChPh, 127, 221106
Agúndez, M., Cernicharo, J., Decin, L., Encrenaz, P., & Teyssier, D. 2014, ApJL, 790, L27
Agúndez, M., Cernicharo, J., Pardo, J. R., Guélin, M., & Phillips, T. G. 2008, A&A, 485, L33
Amyay, B., Fayt, A., & Herman, M. 2011, JChPh, 135, 234305
Bowman, J. M., Jr., Carrington, T., & Meyer, H. D. 2008, MolPh, 106, 2145
Bowman, J. M., Christoffel, K., & Tobin, F. 1979, JPhCh, 83, 905
Carter, S., Bowman, J. M., & Handy, N. C. 2012, MolPh, 110, 775
Carter, S., Wang, Y., & Bowman, J. M. 2017, JPCA, 121, 1616
Cherchneff, I. 2012, A&A, 545, A12
Christoffel, K. M., & Bowman, J. M. 1982, CPL, 85, 220
Clark, V. H. J., Owens, A., Tennyson, J., & Yurchenko, S. N. 2020, JQSRT, 246, 106929
Czakó, G., Mátyus, E., & Császár, A. G. 2009, JPCA, 113, 11665
Darling, B. T., & Dennison, D. M. 1940, PhRv, 57, 128
Dinu, D. F., Tschöpe, M., Schröder, B., Liedl, K. R., & Rauhut, G. 2022, JChPh, 157, 154107
Dinu, D. F., Ziegler, B., Podewitz, M., et al. 2020, JMoSp, 367, 111224
Dunham, T., Jr. 1937, PASP, 49, 26
Endres, C. P., Schlemmer, S., Schilke, P., Stutzki, J., & Müller, H. S. P. 2016, JMoSp, 327, 95
Erfort, S., Tschöpe, M., & Rauhut, G. 2020a, JChPh, 152, 244104
Erfort, S., Tschöpe, M., & Rauhut, G. 2022, JChPh, 156, 124102
Erfort, S., Tschöpe, M., Rauhut, G., Zeng, X., & Tew, D. P. 2020b, JChPh, 152, 174306
Ferenc, D., & Matyus, E. 2019, MolPh, 117, 1694
Fermi, E. 1931, ZPhy, 71, 250
Ghellab, T., Baaziz, H., Charifi, Z., et al. 2019, MRE, 6, 075906
Harris, G. J., Viti, S., Mussa, H. Y., & Tennyson, J. 1998, JChPh, 109, 7197
Jacobs, H., Nymwegen, R., Doyle, S., Wroblewski, T., & Kockelmann, W. 1997, Z. Anorg. Allg. Chem., 623, 1467
Kats, D., & Manby, F. R. 2013, JChPh, 139, 021102
Knauth, D. C., Andersson, B. G., McCandliss, S. R., & Warren Moos, H. 2004, Natur, 429, 636
Knizia, G., & Werner, H.-J. 2008, JChPh, 128, 154103
Lu, B., Shao, X., Jiang, X., et al. 2022, JAChS, 144, 21853
Martin, J., Francois, J., & Gijbels, R. 1992, JChPh, 96, 7633
Mathea, T., Petrenko, T., & Rauhut, G. 2022, JCoCh, 43, 6
Mathea, T., & Rauhut, G. 2021, JCoCh, 42, 2321
May, A. J., & Manby, F. R. 2004, JChPh, 121, 4479
McGuire, B. A. 2018, ApJS, 239, 17
McKellar, A. 1940, PASP, 52, 187
Müller, H. S. P., Schlöder, F., Stutzki, J., & Winnewisser, G. 2005, JMoSt, 742, 215
Müller, H. S. P., Thorwirth, S., Roth, D. A., & Winnewisser, G. 2001, A&A, 370, L49
Neff, M., & Rauhut, G. 2009, JChPh, 131, 124129
Nikitin, A. V., Rey, M., & Tyuterev, V. G. 2017, JQSRT, 200, 90
Peterson, K. A., Adler, T. B., & Werner, H.-J. 2008, JChPh, 128, 084102
Petrenko, T., & Rauhut, G. 2017, JChPh, 146, 124101
Pfeiffer, F., & Rauhut, G. 2014, JChPh, 140, 064110
Pflüger, K., Paulus, M., Jagiella, S., Burkert, T., & Rauhut, G. 2005, Theor. Chem. Acc., 114, 327
Rauhut, G. 2004, JChPh, 121, 9313
Rey, M., Nikitin, A. V., & Tyuterev, V. G. 2017, ApJ, 847, 105
Santa Daria, A. M., Avila, G., & Matyus, E. 2021, JChPh, 154, 224302
Sarka, J., Petty, C., & Poirier, B. 2019, JChPh, 151, 174304
Schneider, M., & Rauhut, G. 2022, JCoCh, 44, 298
Schnick, W., & Lücke, J. 1992, Z. Anorg. Allg. Chem., 610, 121
Schröder, B., & Rauhut, G. 2022, in Vibrational Dynamics of Molecules, ed. J. M. Bowman (Singapore: World Scientific), 1
Simmons, J., Wang, X.-G., & Carrington, T. J. 2019, JPCA, 123, 10281
Smydke, J., Fabri, C., Sarka, J., & Császár, A. G. 2019, PCCP, 21, 3453
Špirko, V., Jensen, P., Bunker, P., & Čejchan, A. 1985, JMoSp, 112, 183
Swings, P., & Rosenfeld, L. 1937, ApJ, 86, 483
Tenenbaum, E. D., & Ziurys, L. M. 2008, ApJL, 680, L121
Tobias, R., Furtenbacher, T., Tennyson, J., & Császár, A. G. 2019, PCCP, 21, 3473
Tschöpe, M., & Rauhut, G. 2022, JChPh, 157, 234105
Tschöpe, M., & Rauhut, G. 2023, MNRAS, 520, 3345
Tschöpe, M., Schröder, B., Erfort, S., & Rauhut, G. 2021, FrCh, 8, 1222
Tyuterev, V. G., Barbe, A., Jacquemart, D., et al. 2019, JChPh, 150, 184303
Vidler, M., & Tennyson, J. 2000, JChPh, 113, 9766
Wang, X.-G., & Carrington, T., Jr. 2013, MolPh, 111, 2320
Watson, J. K. G. 1968, MolPh, 15, 479
Werner, H.-J., Knowles, P. J., Manby, F. R., et al. 2020, JChPh, 152, 144107
Yachmenev, A., Polyak, I., & Thiel, W. 2013, JChPh, 139, 204308
Yachmenev, A., Yurchenko, S. N., Ribeyre, T., & Thiel, W. 2011, JChPh, 135, 074302
Yurchenko, S. N., Amundsen, D. S., Tennyson, J., & Waldmann, I. P. 2017, A&A, 605, A65
Ziegler, B., & Rauhut, G. 2016, JChPh, 144, 114114
Ziegler, B., & Rauhut, G. 2018, JChPh, 149, 164110
Ziegler, B., & Rauhut, G. 2019, JPCA, 123, 3367